The Hebrew University of Jerusalem
Faculty of Mathematics and Sciences
Selim and Rachel Benin School of Engineering
Applied Physics Department

Waveguide Grating Router Phase Trimming for a Fine Resolution Photonic Spectral Processor

תיקוני פאזה באמצעות צריבה במערך מוליכי גלים המיועד למעצב אופטי בעל כושר הפרדה גבוהה

by

Noam Goldshtein

This work was done under the supervision of

Prof. Dan M. Marom

Thesis submitted for a M.Sc. degree

November, 2015

Abstract

Spectrally dispersed light from a fine resolution waveguide grating router (WGR) of 25 GHz free spectral range (FSR) that radiates to free-space is spatially filtered at ~1 GHz resolution using a liquid crystal on Silicon (LCoS) spatial light modulator (SLM). Fabrication imperfections leading to phase errors on the 32 waveguide arms of the WGR are measured by the pair-wise far-field interference of adjacent waveguide pairs. The phase errors are then corrected using a UV pulsed laser to inscribe permanent optical path changes to the waveguides. WGR phase errors are permanently trimmed waveguide-by-waveguide with an excimer laser by inducing stress in the glass cladding above the waveguide for coarse setting and using the photosensitivity effect for fine setting. The WGR was then mated with an LCoS SLM located at the Fourier plane to form a photonic spectral processor (PSP), for arbitrary spectral amplitude and phase manipulations.

תקציר

מערך מוליכי גלים בעל חלון ספקטרלי מחזורי של 25 גיגה הרץ וכושר הפרדה גבוהה המקרין לאוויר החופשי משמש לדיספרסיה של אור העובר פילטור ספקטרלי ברזולוצייה של 1 גיגה הרץ ע"י מאפנן אור מרחבי (גביש נוזלי על סיליקון). פגמי ייצור גוררים שגיאות פאזה ב32 הזרועות של המערך, אשר נמדדות בעזרת תבנית ההתאבכות בשדה הרחוק של זוגות צמודים של מוליכי גל. שגיאות הפאזה שנמדדו מתוקנות ע"י לייזר אולטרא-סגול היוצר שינויים קבועים בדרך האופטית. שגיאות הפאזה מתוקנות ע"י צריבת כל מוליך גל בנפרד, כאשר הסטות פאזה גסות נעשות ע"י יצירת מאמצים בחיפוי הזכוכית שמעל למוליך הגל, והסטות פאזה עדינות נעשה ע"י אפקט הפוטוסנסטיביות. מאפנן אור מרחבי הממוקם במישור הפורייה של המערך המתוקן יוצר מעצב אופטי בעל רזולוצייה חדה המאפשר ביצוע מניפולציות ספקטרליות שרירותיות על המשרעת והפאזה של האות הנכנס.

Acknowledgments

I would like to thank my advisor Prof. Dan M. Marom, whose guidance and expertise has made this achievement possible.

I would also like to thank Leonid Pascar, David Sinefeld, Dror Shayovitz, Ori Golani, and all other members of our photonic lab group for their helpful support. I learned a lot from our collaborated work, and I hope we will have the opportunity to work together again someday.

Table of contents:

1. Introduction

Planar lightwave circuit (PLC) waveguide grating router (WGR) based systems are commonly used in modern optical communications, mainly as multiplexers and demultiplexers. A special class of spectral processing devices uses a unique WGR design with unconventional output; instead of employing a second slab-lens region that demultiplexes to individual output waveguides, the grating arms terminate at the PLC edge and the light radiates to free-space, forming a phased array exhibiting angular dispersion. The diffracted, angularly dispersed light is converted by a Fourier lens to spatially dispersed light at the lens back focal plane, where it may be manipulated by a spatial light modulator (SLM), employing either MEMS micromirrors [1]-[2] or liquid crystal on Silicon (LCoS) pixels [3]-[4] (Fig. 1). Such hybrid guided-wave / free-space optics processors can serve as a more compact realization of a wavelength-selective switch than a conventional bulk grating design [5]-[6]. The WGR-based dispersive optics further provide a wider design space that can achieve finer optical resolving power, enabling intra-channel spectral filtering applications [7]-[9], giving the fine filtering apparatus the moniker photonic spectral processor (PSP). WGR-based components critically depend on the phase accuracy of the embedded waveguide array [10], yet measuring these phase errors in components such as multiplexers is not trivial as the measurement is indirect [11]. This becomes especially challenging for fine resolution WGR based devices, as the waveguide path length difference increases. A 1 GHz spaced demultiplexer had to employ waveguide trimming in order to correct for phase errors [12]. The WGR our group designed suffered from fabrication phase errors rendering the device inoperable unless the phase errors were corrected. Here we expand on our paper on a PSP employing a WGR for fine resolution spectral separation, where a permanent phase trimming technique to the WGR has been directly applied with an excimer laser, correcting for the fabrication phase errors [13]. The optical setup is thus greatly simplified and simply consists of the trimmed WGR, a Fourier lens and single LCoS SLM for spectral manipulations (Fig. 1). The trimmed WGR used in this experiment has a 25 GHz FSR and is intended to serve as fine WDM interleaver (12.5/25 GHz) of an OFDM-PON network project [15].

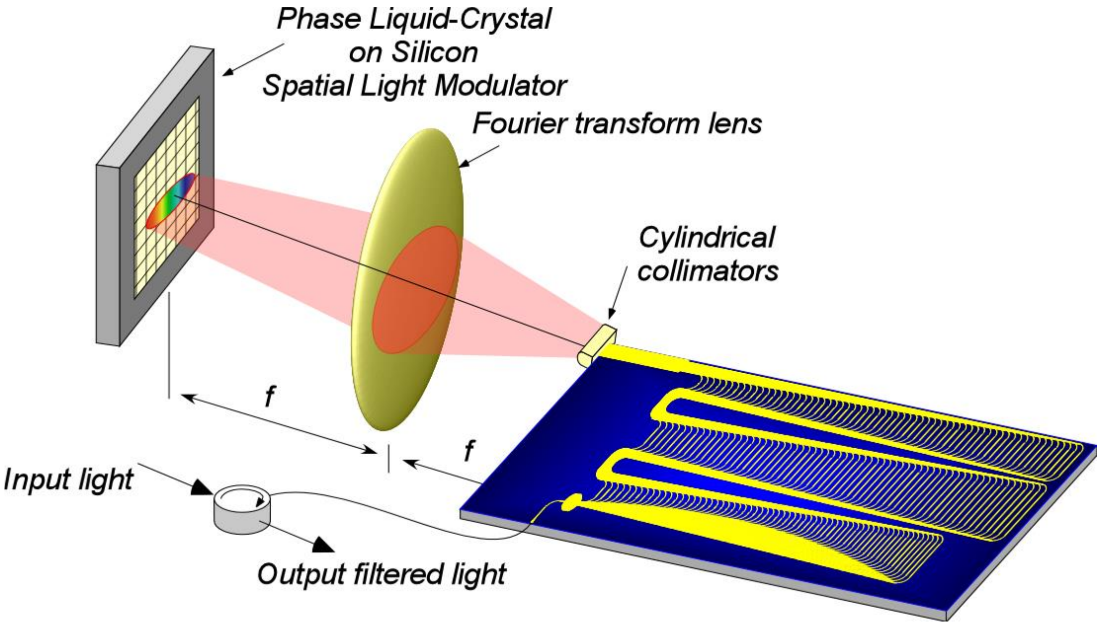

Figure 1. Hybrid guided-wave/free-space optics dispersive platform with LCoS SLM for spectral manipulation.

2 Background

2.1 Fine Resolution Waveguide Grating Router Design

A conventional WGR demux uses a waveguide array with a constant length increment to diffract an input signal into several waveguide outputs. An input waveguide radiates via a free space propagation region (first star coupler) into the waveguide array, where each waveguide accumulates a different phase shift on account of the incremental optical path lengths. The array radiates into a second free space propagation region (second star coupler) where the dispersed light emerging from the waveguide array is coupled to individual demultiplexed output waveguides (Fig. 2.1.1).

The WGR we use is unconventional—we discard the second slab lens region that demultiplexes to output waveguides. The grating arms terminate at the PLC edge, allowing the light to radiate into free space. This forms a phased-array output that experiences angular dispersion on account of wavelength-dependent phase delays in the waveguide array. Using an external Fourier lens, we obtain spatially dispersed light allowing for manipulation in free space with an SLM as shown in Fig. 1. The key design features of a WGR are its incremental path length increase, ΔL, between successive waveguides and number of waveguides, N, within the array. The former sets the FSR according to $\Delta v_{FSR} = c/(n_g \cdot \Delta L)$ (where n_g is the group index of the waveguide propagating mode and c is the speed of light) and the latter sets the spectral resolution $v_{res} \cong \Delta v_{FSR}/N$. The WGR we discuss here is designed to provide fine resolution by limiting the overall bandwidth to a 25 GHz FSR (small Δv_{FSR}). It was fabricated with N=32 waveguide arms with a relative path length of $\Delta L = m \cdot \lambda_0 / n_{eff}$=~8 mm (where

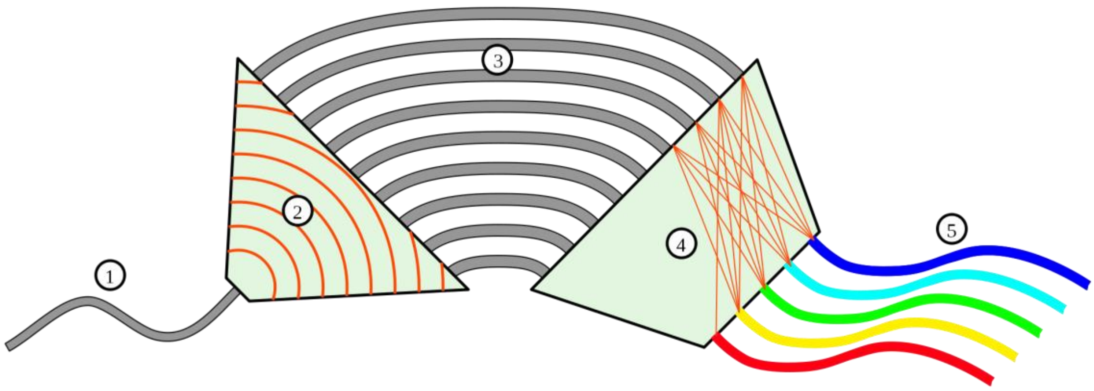

Fig. 2.1.1 –Conventional WGR schematic: Light from an input waveguide (1) radiates into a star coupler (2) and coupled to a waveguide array of incremental length (3). The array radiates into a second star coupler (4) where the light interferes at the entries of the output waveguides (5), coupling different wavelengths into different outputs.

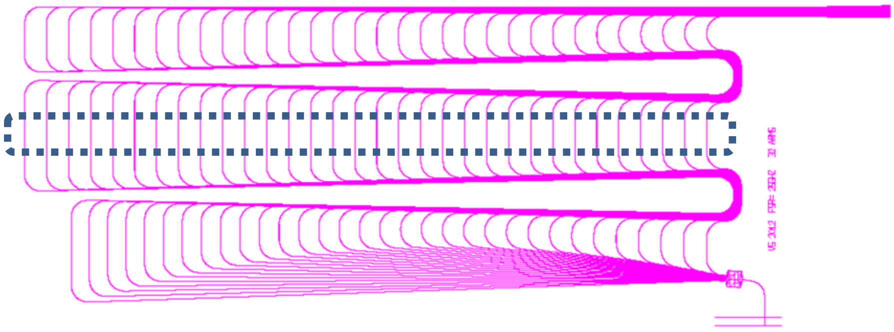

Figure 2.1.2 Waveguide grating router with sub-1 GHz optical resolution design layout (dimensions ~2×5.5 cm). Dashed line indicates designed trimming zone, where parallel waveguides are well separated and a few mm long.

m=7480 is the diffraction order and n_{eff} is the waveguide effective index), for a total WGR path length difference of $N\cdot\Delta L$~250 mm. The inverse of the time delay ($\Delta t=N\cdot\Delta L/v_g$=1.25 ns) matches our 0.8 GHz target resolution, in line with time-bandwidth uncertainty principle. The WGR was implemented in a silica on silicon platform with 2% index contrast waveguides of 4×4 µm cross-section (Fig. 2.1.2) with $n_{eff}\cong$1.46. To obtain a compact WGR design for such a long path difference, the waveguides are folded three times within the PLC (total size is 2×5.5 cm). The WGR has a designated trimming area (Fig. 2.1.2), where each waveguide has a straight segment suitable for trimming of at least 2.2 mm length, with a 1.3 mm separation between waveguides. The waveguide pitch at the output (at the PLC edge) is 18.6 µm, and the waveguides are adiabatically broadened to size Δ_{wg}=17 µm. The challenge in realizing such WGR is maintaining the phase accuracy across the entire array, as phase errors will at first lower the resolution and then completely ruin the WGR performance if approaching or exceeding π (Fig. 2.1.3). Many factors may contribute to the sources of phase errors, such as lithography/etching errors, core height variations, refractive index inhomogeneity and/or stress.

The choice of the WGR as the dispersive element is due to the need for high resolution and a strong spectral dispersion. Diffraction gratings are limited by their periodic structure and feature size, leading to a limited amount of spectral dispersion. While virtually imaged phased arrays (VIPA) are able to deliver the desired resolution and dispersion [14], they exhibit low coupling efficiency to single mode fibers that is intrinsic to their method of operation, and are difficulty to integrate it in a small scale system, i.e. on-chip systems.

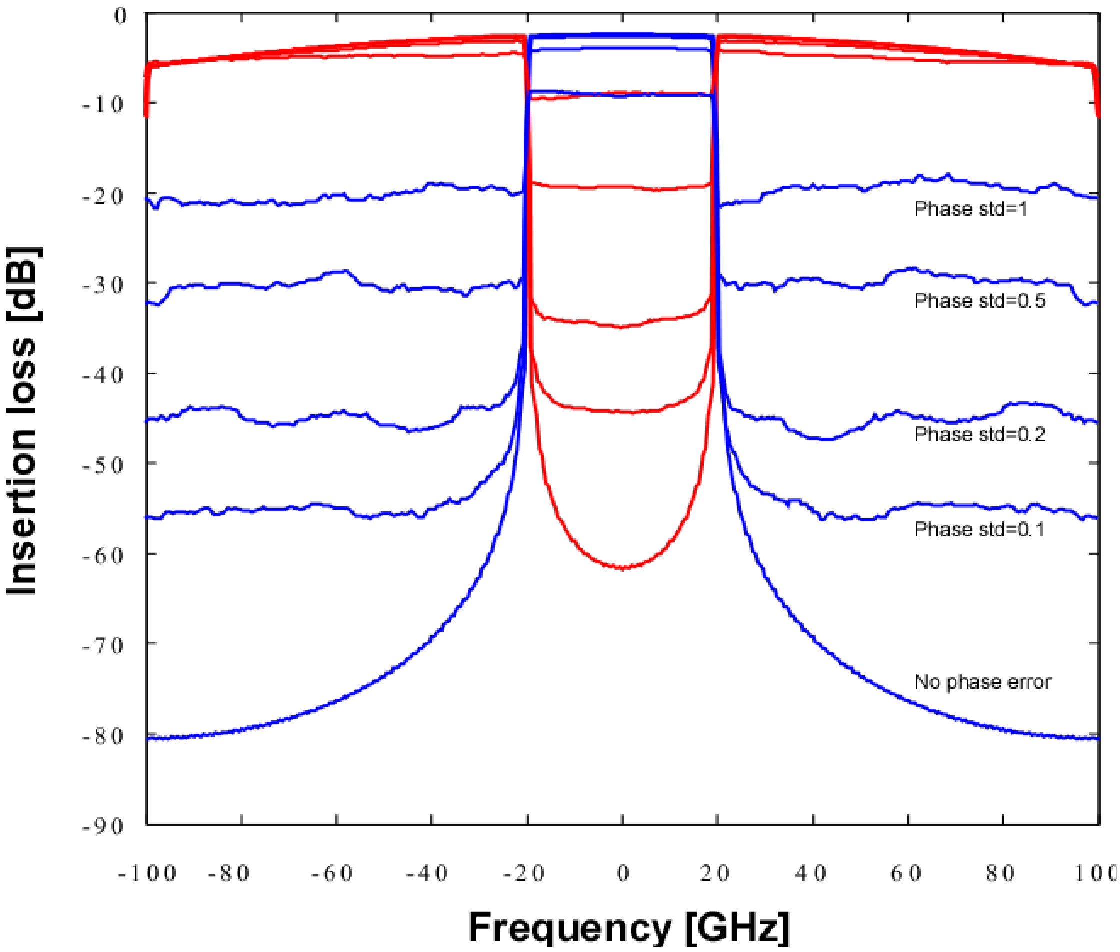

Figure 2.1.3 Simulations done on a different design of sub-1 GHz optical resolution WGR, with 250 arms and 200 GHz FSR, illustrating the degradation of a pass (blue) and block (red) filter capabilities with growing WGR phase errors.

2.2 Photonic Spectral Processor

Optical devices that perform signal conditioning and controlling on WDM traffic are important for maximizing the performance of optical communication systems. Channel power equalizers are required for maintaining the same OSNR across all amplified channels in a long-haul system, and dispersion compensators are essential in communication systems employing direct or differential detection, and can reduce the digital processing overhead in coherent reception systems.

A device we call a photonic spectral processor (PSP) achieves all of the above, using spatial dispersion to separate the light's frequency components onto a spatial light modulator (SLM) which applies an adaptive filtering function [7] (Fig 2.2.1). A high resolution dispersive element is needed to construct a PSP for high rate optical communication signals. The optical performance of such spectral processing devices depends on the dispersing optics' spectral resolution, and the SLM's spectral addressability.

A finer resolution PSP allows more abrupt transitions from pass to block bands as a result of finer filtering, a trait instrumental for densely packing channels in the telecom optical window (1525-1560nm), imposed by current optical amplification technology. The guard bands necessary to prevent coherent crosstalk are roughly equivalent to the transition bandwidth from pass to block bands, and a finer resolution PSP enables to minimize them.

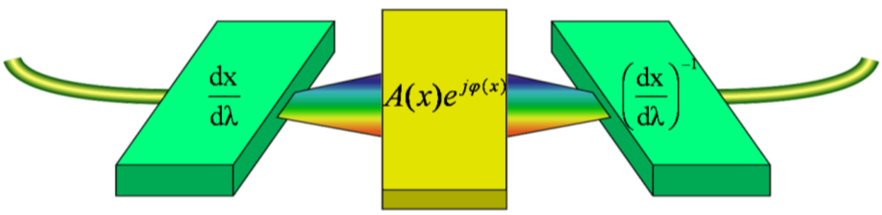

Figure 2.2.1 Concept of a Photonic Spectral Processor: Input signal traverses a dispersion element and a Fourier lens to form a spectral spread on a real plane. A spatial light modulator placed in this plane enables phase and amplitude modulation for each spectral component. The spectrally manipulated is then coupled to an output fiber. Note that this is a schematic representation to the system described in Figure 1.

The dispersed optical signal can be described by:

$$\varphi(x;\nu) = \exp\left[-\left(x - \frac{dx}{d\nu}(\nu - \nu_0)\right)^2 \Big/ w_0^2\right] \qquad (2.2.1)$$

Each spectral component is focused to a spot size of $2w_0$ at a unique position, and the spectra is linearly dispersed as defined by dx/dv. The Drop function is implemented by passing some spectral components while blocking others. Allowing a bandwidth occupying a spatial extent Δx about the origin and performing the overlap integral over the spatial coordinate x yields the coupling strength for every spectral component. This enables us to evaluate the spectrally-dependent power coupling (remembering that $\Delta x = (dx/dv)\cdot\Delta v$):

$$\begin{aligned}\left|\varphi(\nu)\right|^2 &= \frac{1}{4}\left(\operatorname{erf}\left[\frac{\sqrt{2}}{w_0}\left(\frac{\Delta x}{2} + \frac{dx}{d\nu}(\nu - \nu_0)\right)\right] + \operatorname{erf}\left[\frac{\sqrt{2}}{w_0}\left(\frac{\Delta x}{2} - \frac{dx}{d\nu}(\nu - \nu_0)\right)\right]\right)^2 \\ &= \frac{1}{4}\left(\operatorname{erf}\left[\frac{\sqrt{2}}{w_0}\frac{dx}{d\nu}\left(\frac{\Delta\nu}{2} + (\nu - \nu_0)\right)\right] + \operatorname{erf}\left[\frac{\sqrt{2}}{w_0}\frac{dx}{d\nu}\left(\frac{\Delta\nu}{2} - (\nu - \nu_0)\right)\right]\right)^2\end{aligned} \qquad (2.2.2)$$

Each error function defines the spectral roll off at the corresponding spectral edge, when the two edges are sufficiently separated.

Assumption that the bandwidth selected is wide and each error function defines the roll off independently, we define the spectral resolution by measuring the bandwidth of the 90% to 10% transition (corresponding to -0.5dB to -10dB transition bandwidth, see Fig. 2.2.2-left). The difference in the two erf(•) arguments is 1.436, so $\left(\sqrt{2}\cdot dx/d\nu\right)\big/w_0$ is equal to 1.436/ν_{res}, or $\nu_{res} \approx w_0/(dx/d\nu)$, and we can rewrite:

$$\left|\varphi(\nu)\right|^2 = \frac{1}{4}\left(\operatorname{erf}\left[\frac{1.436}{\nu_{res}}\left(\frac{\Delta\nu}{2} + (\nu - \nu_0)\right)\right] + \operatorname{erf}\left[\frac{1.436}{\nu_{res}}\left(\frac{\Delta\nu}{2} - (\nu - \nu_0)\right)\right]\right)^2 \qquad (2.2.3)$$

where ν_{res} is the 10-90 bandwidth. This quantity is easy to identify and measure, as shown in Fig. 2.2.2. We can now related the resolution to bandwidth occupied by deeper transitions, such as down to -20 dB, requiring 1.4·ν_{res}, or to the transition at -30 dB requiring 1.667·ν_{res} (see Fig 2.2.2-right). If we wish to maintain -40dB isolation, we can adopt a 1.9·ν_{res} metric for WDM signal separation, which can be rounded to 2·ν_{res} with a safety margin.

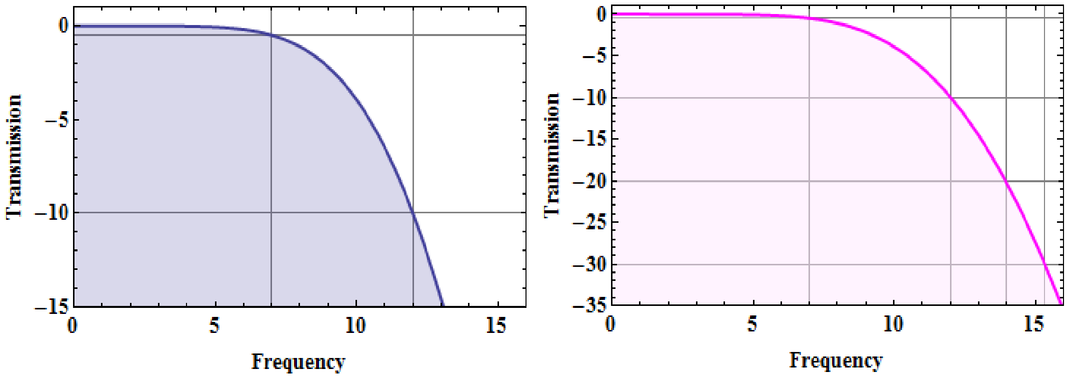

Figure 2.2.2 Characterizing the optical resolution of the filter shape, by measuring the bandwidth for the transition from -0.5 dB to -10 dB (equivalent to the 90-10 drop bandwidth). Horizontal grid lines at -0.5 dB and -10 dB demonstrate a 5 dB optical resolution (from 7 GHz to 12 GHz). Right: Additional measures added at -20 dB and -30 dB, at 1.4×5=7 GHz, and 1.66×5=8.33 GHz.

In addition to the resolution metric, a PSP is also characterized by the positional accuracy at which it is possible to encode a spectral function on the LCoS SLM. This positional accuracy is defined as the spectral addressability. Knowing the spatial dispersion term dx/dν and LCoS pixel size p, the spectral addressability is p/(dx/dν).

In summary, the channel passband shape is determined by the optical resolution, whereas the spectral addressability at which channel bandwidths can be assigned is defined by the SLM size and the spatial dispersion

3 Experimental Setup and Results

3.1 Phase Error Measurement

Our WGR with a radiating output allows direct access to the waveguides at the output facet, in contrast to fully integrated multiplexers. This allows us to devise a direct phase measurement technique, rather than relying on Fourier transform spectroscopy techniques and their associated sensitivity to noise impacting the calculations [11]. In order to obtain phase error information, we block the output facet of the WGR with a spatial mask which contains a slit wide enough to span two adjacent waveguides. The light that emerges from the mask is split in the vertical direction, with one part being imaged and the other Fourier transformed- both onto an IR camera (see Fig. 3.1.1). The former is used to position the mask, moving it relative to the WGR until two equal spots are imaged onto the camera. This ensures us that only two waveguides contribute to the formed interference pattern. In order to ease the tolerances, we use a relay imaging arrangement to enlarge the waveguides image. This simplifies the placement of the slit, as it is placed on the magnified waveguide image. The optical relay system is composed of a Mitutoyo X10 NIR objective with a focal length of 20 mm, and a 100 mm tube lens, resulting in a magnification of 5. As a Fourier lens we used a 50 mm focal length

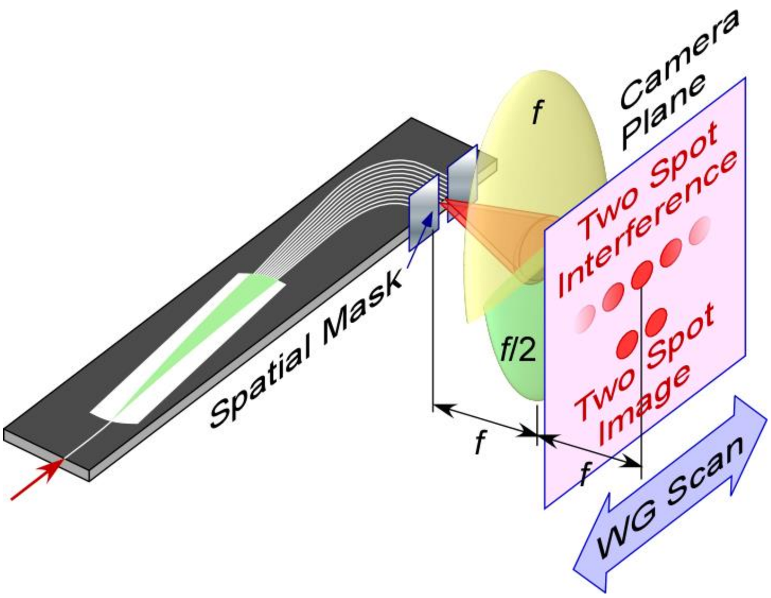

Figure 3.1.1 Layout of the WGR phase errors evaluation system and UV trimming. A slit placed at the WGR output selects two adjacent waveguides whose output is split into two vertical sections, both imaged onto the same IR camera. The upper part is incident on a Fourier lens to form an interference pattern containing the phase error information, and the lower part is imaged (with a 4f arrangement) for centering the slit on the WG pair. Lateral scanning of the measurement system across the WGR output allows scanning of all the waveguides pairs.

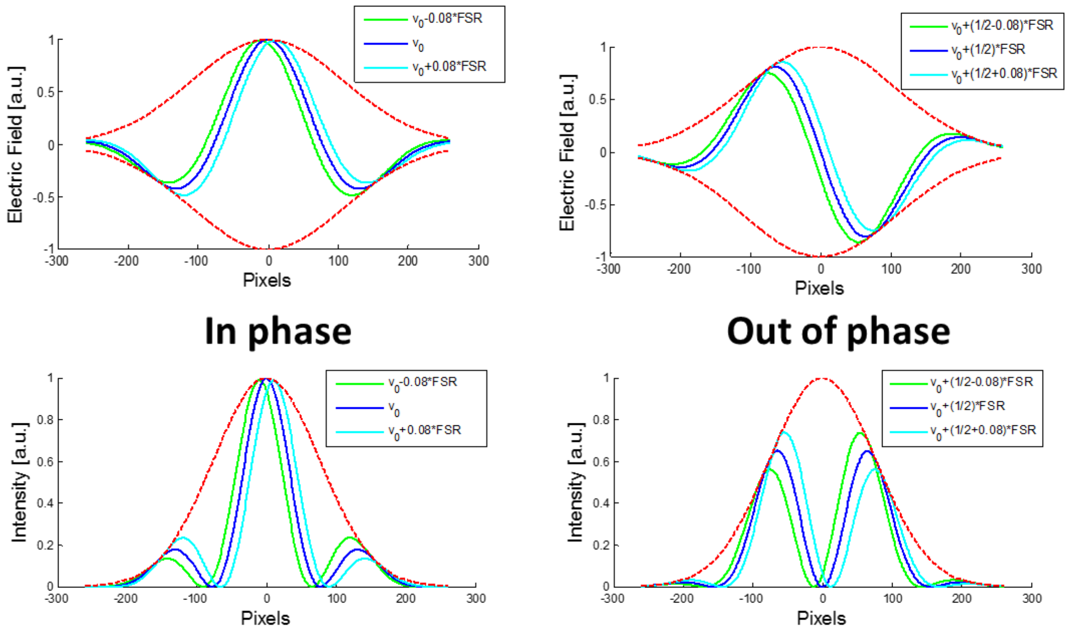

Figure 3.1.2 Far-field interference simulation of a waveguide pair, illustrating the change in electrical field and intensity with varying wavelength, near the in-phase and out-of-phase conditions. In our set-up we measure the energy difference between the two lobes of the out-of-phase interference pattern, which is the most sensitive position for estimating the phase error (waveguide Gaussian envelope in red).

cylindrical lens and as the imaging lens a 25 mm focal length cylindrical lens, which were glued together to simplify placement.

The radiating light from the two waveguides interferes in the far field, resulting in a pattern which depends on the relative phase between the two waveguides (Fig. 3.1.2). The phase difference between the two waveguides under test can be obtained by the interference fringe shift (This is identical to Young's double slit diffraction pattern). Scanning along all the output waveguides provides the relative phase between each pair of waveguides.

From a single interference image it is difficult to obtain a high fidelity measurement of the phase difference. Hence, we use an additional degree of freedom at our disposal, tuning the interrogating monochromatic laser wavelength exciting the waveguide array. Since the WGR has an incremental length difference between every two waveguides, scanning the wavelength across the WGR FSR is identical to adding a phase modulation on the longer waveguide that we can tune at will. When the two waveguides radiate in phase, the far-field interference pattern results in the formation of one major lobe in the far field under the envelope of the individual waveguide far field diffraction pattern.

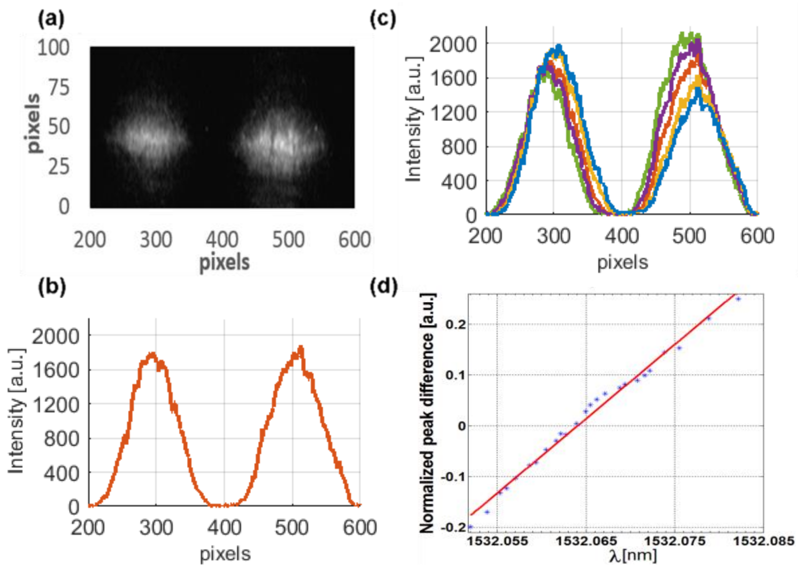

Figure 3.1.3 Wavelength sweep algorithm. (a) Image of far-field interference pattern at the Fourier plane, near equal peaks condition. (b) Lobe intensity showing equal power between the two interference lobes. (c) Lobe intensity for different wavelength excitation. (d) Normalized peak difference calculated for each wavelength during the scan. From the linear fit of the scanning results λ_{eq} is extracted.

This, however, is the most insensitive position for estimating the phase error in one of the waveguides, as tracking small changes in the main lobe position is quite difficult in the presence of noise associated with phosphorus coated CCD cameras (see Fig. 3.1.3-a). Instead, we tune the laser until both waveguides are π out of phase. In this case, the far field radiation pattern is of two equal lobes (residing within the waveguide radiation envelope). Small phase errors result in one lobe increasing and the other decreasing, and we can tune the laser to the wavelength at which the lobes are equal (Fig. 3.1.3-b).

The wavelength identified, λ_{eq}, is now a measure of the waveguide phase error. Let us assume there is a phase error, θ_{err}, in the waveguide. Hence the phase difference between two waveguides at the design wavelength, λ_0, is characterized by

$$k\left(\lambda_0\right)\Delta L = 2\pi m + \theta_{err} \quad (3.1.1)$$

When we tune the laser source to identify the wavelength that results in the two waveguides being π out of phase, we satisfy

$$k\left(\lambda_{eq}\right)\Delta L = 2\pi m - \pi \quad (3.1.2)$$

Taking the difference of Eqs. (3.1.1) and (3.1.2) and approximating the wavevector difference by the product of the wavevector derivative and the wavelength shift, we obtain

$$\left[k\left(\lambda_{eq}\right) - k\left(\lambda_0\right)\right]\Delta L \approx \frac{dk}{d\lambda}\cdot\left(\lambda_{eq} - \lambda_0\right)\Delta L = -\pi - \theta_{err} \quad (3.1.3)$$

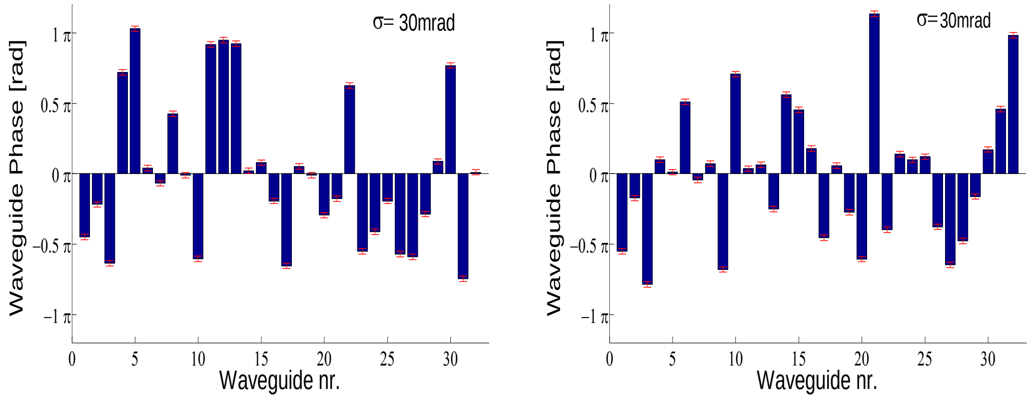

Figure 3.1.4 Phase errors of the WGR horizontal (Left) and vertical (Right) polarizations.

Using the definition for the WGR's FSR we can simplify Eq. (3.1.3) and obtain a direct measure of the phase error:

$$\theta_{err} = 2\pi \frac{\lambda_{eq} - \lambda_0}{\Delta\lambda_{FSR}} - \pi \qquad (3.1.4)$$

We now see that the phase error is linear with the deviation of λ_{eq} from the WGR's designed center wavelength. Note that we cannot distinguish errors of multiple orders of 2π. However, the technique sets the right phase for the design wavelength, λ_0, regardless of the erroneous order. Such an error will manifest itself in distant diffraction orders, when the accumulated phase is slightly off. However, this phase error on other diffraction orders scales as the ratio of the number of 2π cycle slips (error) to the designed diffraction order, *m*. Since *m*=7480 in our case, we are insensitive to multiple orders of 2π cycle slips, assuming they are small.

A fully automated WGR scanning and evaluation procedure has been developed, by placing the free-space optical measurement system on a moving stage. We assessed the accuracy for the measurement system with the 25 GHz FSR WGR by 50 repeated measurements. We report an average error of 30 mrad for the entire system, larger than our previously reported figure in [16], where a similar measurement system obtained 13 mrad measurement error and the FSR was 5 THz. Our current error is larger due to switching to a WGR with a smaller FSR, and the wavelength accuracy of the scanning laser starts to become the limiting factor.

In order to account for the two orthogonal polarizations, a polarizer was placed before the imaging and Fourier lens, enabling an independent measurement of each polarization. We found our WGR exhibits birefringence and weak correlation between the errors in the two polarizations (Fig. 3.1.4), meaning a polarization diverse phase correction is required.

After measuring relative phases between all adjacent waveguides, we need to identify an optimized waveguide trimming strategy for minimum writing time. A degree of freedom at our disposal is the choice of absolute output phase, as it does not impact the WGR function. This is done by successively choosing each waveguide of the array to be the reference waveguide, and assessing the total accumulated phase that has to be inscribed to all other waveguides in order to achieve the equal phase property. The optimized strategy is the one that requires the least amount of accumulated phase writing.

3.2 Phase Error Compensation

To correct the phase errors introduced in fabrication we employed a phase trimming procedure applied post fabrication (Fig 3.2.1),. The phase trimming was originally designed around the photosensitivity effect, which occurs for Ge-doped silica when photoexcited with light around 240-250 nm [17]. The photosensitivity effect is stronger with higher concentrations of Ge dopant [18]-[19], which is one of the reasons we designed the WGR with a high index contrast. In addition, the photosensitivity effect is greatly enhanced when the glass matrix is in-diffused with hydrogen. We've tried to quantify this and have seen the expected great improvements in refractive index change [16]. However, hydrogen is in-diffused at high pressure over long time; but when removing the WGR from the high pressure vessel the hydrogen quickly out-diffuses since the over cladding is 12 μm thick only (within an hour in general). This out-diffusion time is much faster than the phase trimming time for the complete WGR, so this approach did not meet our requirements. Without hydrogen loading the photosensitivity effect gave us only ~0.6 rad of phase trimming ability for our available waveguide length in the exposure zone (Fig 3.2.2.a), whereas we require up to 2π trimming range. However, over prolonged exposure to UV energy, the absorbed UV light in the silica glass cladding causes a dilation in the glass and the formation of a

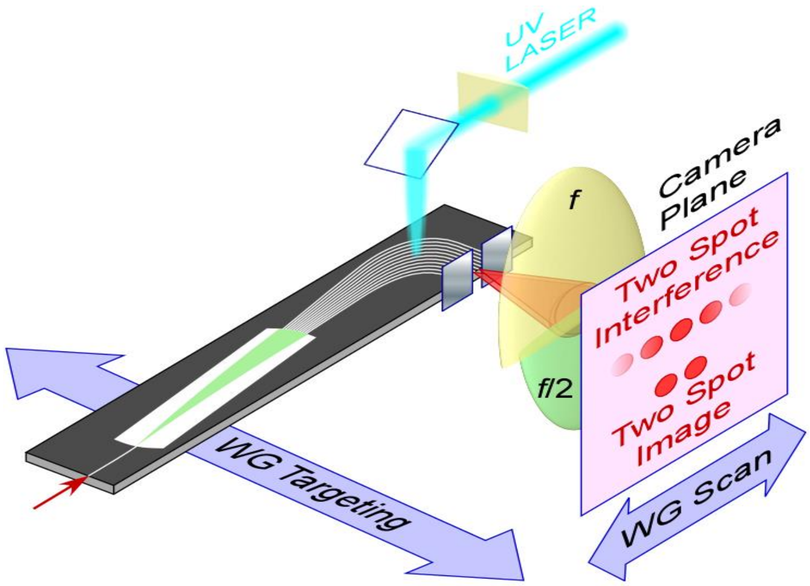

Figure 3.2.1 Layout of the WGR UV trimming set up. The UV beam individually irradiates the waveguide arms to a dose required to adjust the output phase, using feedback from the phase evaluation system. Both WGR and phase evaluation system are mounted on a stage that moves relative to the UV laser, enabling targeting of different waveguides without losing the phase evaluation abilities.

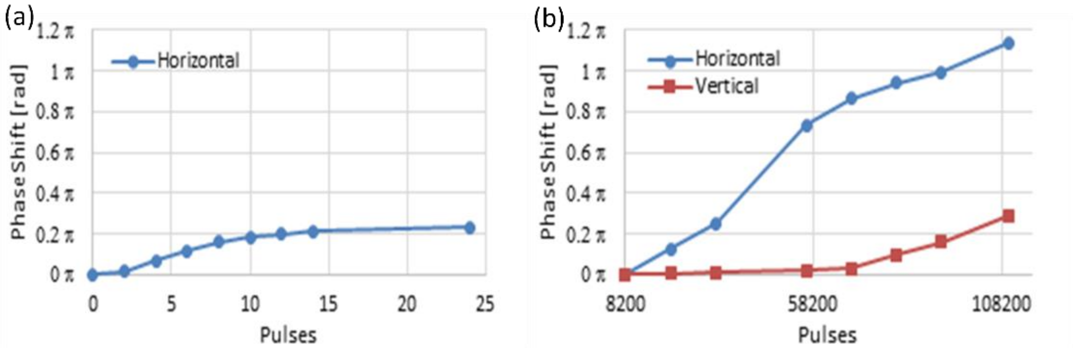

Figure 3.2.2 Phase shift vs Trim Energy of a waveguide pair for photosensitivity effect (Left) and stress effect (Right). Photosensitivity uses a fraction of the energy needed for the same phase shift as stress, but reaches saturation after ~0.6 rad. Stress shows high linearity and no saturation, and phase shifts larger than the required 2π were reached.

local positive index change resulting from the stress [20]. We confirmed the glass dilation by measuring with a Dektak stylus profiler the surface topography of an illuminated cladding area (Fig. 3.2.3.c). The stress in the dilated cladding above the waveguide results in very large phase delays due to the photoelastic effect (Fig 3.2.2.b) [21], and provided us with the necessary phase controls. It should be noted that as the formed stress gradient results in different delays for each polarization (Fig 3.2.2.b)[22], this solution requires a polarization diversity arrangement. We trimmed with laser pulses from an KrF excimer laser (248 nm), focused on the individual waveguides with a cylindrical lens and a metal mask with a rectangular aperture (Fig 3.2.4). Waveguide targeting was aided by an overhead camera monitoring system, viewing through a dichroic mirror that guided the UV laser downwards.

Unlike photosensitivity, stress induced phase shifts undergo stress relaxation (Fig. 3.2.5). We identified two stress relaxation mechanisms impacting the inscribed stress field, one which occurs immediately after the PLC mounting vacuum is released, and another related to relaxation in the glass over time. We addressed the vacuum related relaxation by bonding the PLC to a 3 mm thick Borosilicate glass buffer, as it also

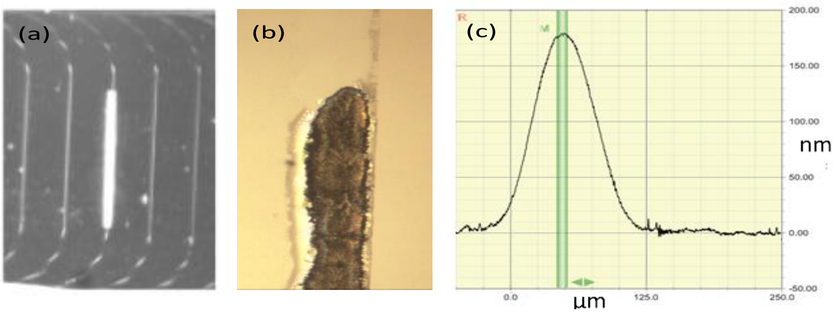

Figure 3.2.3 Glass dilation caused by UV laser absorption in the silica cladding: (a) Camera top-view of a trimmed waveguide. The bright zone is scattered illumination light from the exposed surface; (b) Microscope image of dilated spot on a clear wafer region (no waveguide underneath); (c) Surface topography cross section measured along the narrow dimension of the dilated spot in (b). The formed stress gradient results in phase modulation via the photoelastic effect.

Figure 3.2.4 Trimming mask: Waveguides top view without (left) and with mask (right). The two oval slits enable aiming by locking on neighbor waveguides. UV laser trims the waveguide through the center rectangular slit, which is also used for truncating the beam's long dimension to avoid crosstalk, and spot detection via glow (UV spot is not visible on Silicon).

shares the same thermal expansion coefficient as the Silicon substrate.

The glass relaxation was dealt by trimming the waveguides over several cycles, until the system reached stress equilibrium. Generally three writing cycles were required, with a waiting time of two weeks in between. Thermal annealing may expedite this wait time. Figure 3.2.5 shows the measured WGR horizontal polarization phase errors for the design wavelength before and after initial phase trimming, and after a two week

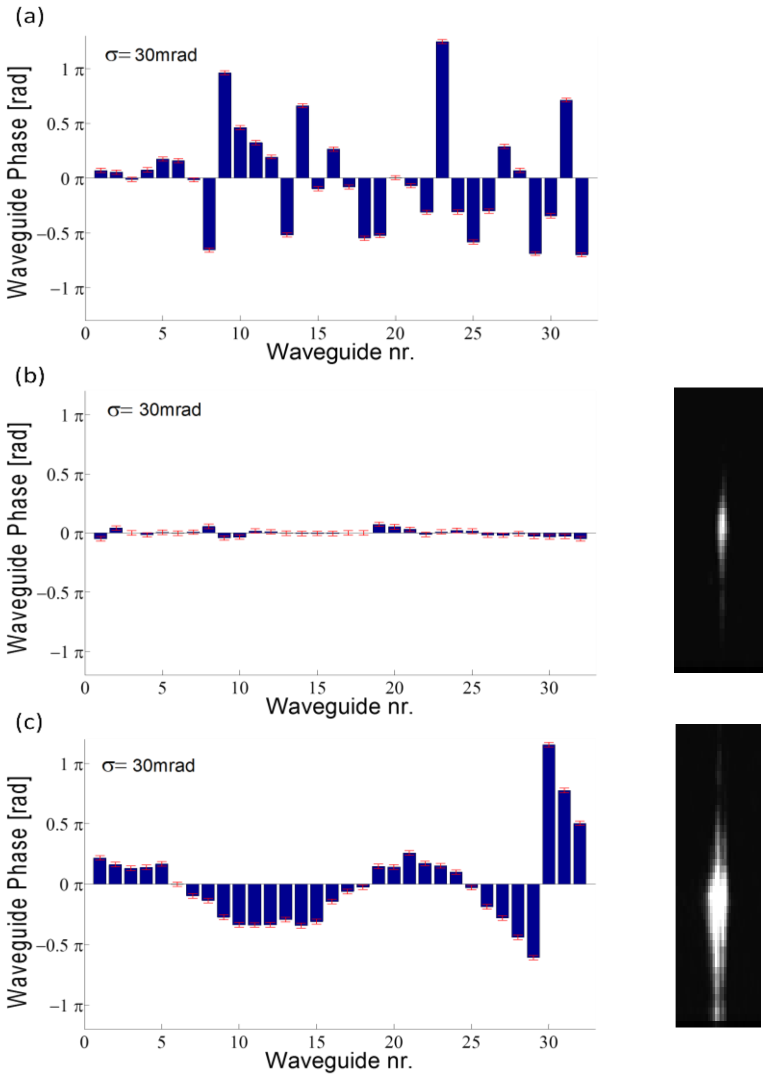

Figure 3.2.5 Phase errors of the WGR horizontal polarization: (a) before trimming, (b) after trimming, and (c) after two weeks and phase relaxation. The effect of stress relaxation is shown by phase measurements as well as Fourier plane pictures taken right after the trimming (b) and two weeks later (c).

relaxation period. What starts out as almost random (though very stable) phase values with no relative relationship, are brought to the same target value.. Even though the phase trimming is not perfect, the performance is good enough to have fine spectral selectivity in the Fourier plane, and no degradation has been observed over several months after repeating the trimming process three times.

3.3 Photonic Spectral System for Fine Resolution Filtering

We assembled the filtering setup and prescribed different filtering functions with the LCoS SLM. This is done by placing the LCoS SLM at the Fourier plane of the WGR and reflecting the modulated light back to the WGR and output fiber. The SLM was placed at a slight tilt diverting all light out the optical path (to eliminate the cover glass back reflection and the second polarization). A linear phase ramp function was written on the SLM in order to steer back selected spectral components with desired attenuation and phase. Since each spectral component radiating into free space from the waveguide array excites few diffraction orders, we back reflect them all to collect all the energy.

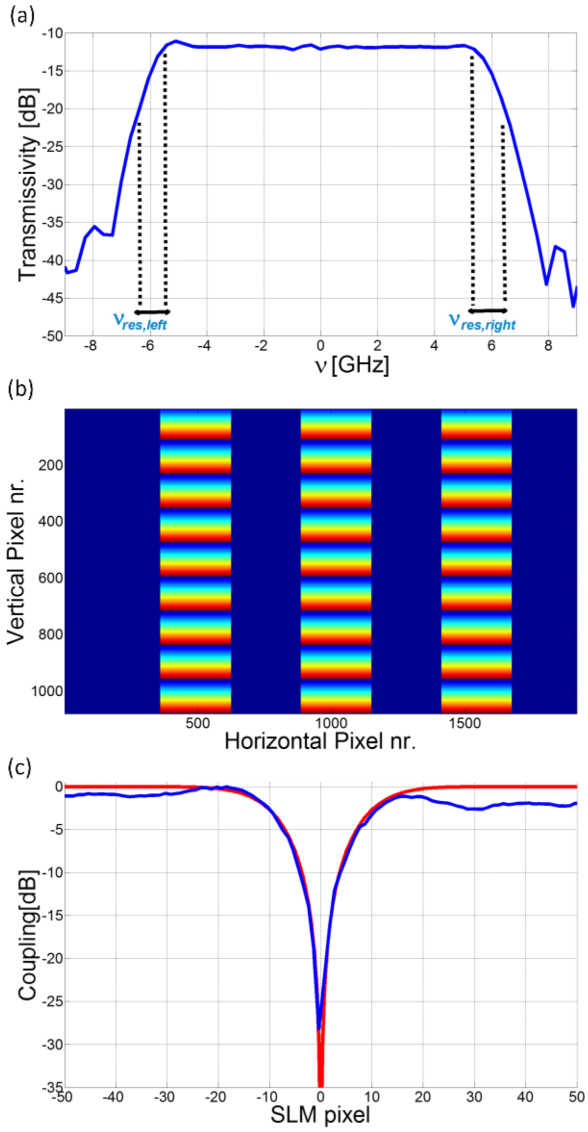

Figure 3.3.1 (a) Resolution metrics of ~1 GHz measured from -0.5 dB (10%) down to - 10 dB (90%). (b) Phase function written to the SLM, for selecting 12.5 GHz band, including higher order diffraction orders. (c) Spot size measurement (300 μm), by scanning a 0-Pi phase transition across the monochromatic spot with the LCoS modulator (Gaussian model fit in red).

This is done by repeating the frequency selection pattern on the SLM with offsets corresponding to the diffraction orders (Fig. 3.3.1.b). Selecting a frequency band in this manner achieves uniform performance no matter where the frequency band occurs with respect to the center frequency of the WGR.

Any bandwidth selection can be prescribed by appropriate control of the SLM. We study the passband features using a swept laser technique, as any optical spectrum analyzer does not have sufficient spectral resolution. The passband edge assessments show that the 90%-10% transitions occur at 1.3 GHz resolution on one side and 0.9 GHz resolution on the other side, indicating that the spot size is slightly asymmetric (Fig. 3.3.1.a) Nevertheless, the optical filtering performance is extremely sharp and suitable for the OFDM-PON application [15] which calls for transitions from pass to block bandwidth of 3.125 GHz. We apply the interleaver functionality and block out 12.5 GHz slices as well as flexible bandwidth carving (Fig. 3.3.2).

In addition to the resolution metric, a PSP is also characterized by the positional accuracy at which it is possible to encode a spectral function on the LCoS SLM. This

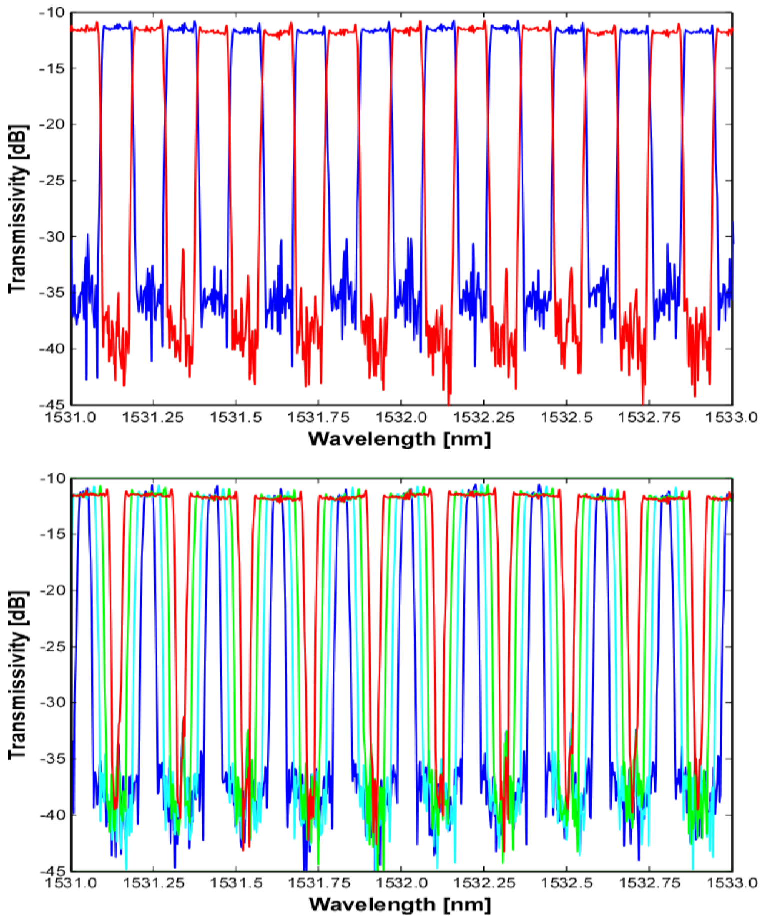

Figure 3.3.2 Top: 12.5/25 GHz interleaver functionality. Bottom: Flexible selection of bandwidth: 5, 10, 15, and 20 GHz wide passbands.

positional accuracy is defined as the spectral addressability. Knowing the spatial dispersion term dx/dν and LCoS pixel size p, the spectral addressability is p/(dx/dν). In our PSP implementation the LCoS pixel size is 8 μm (Holoeye Pluto, 1920×1080 pixels) and the spatial dispersion equals 160 μm/GHz, yielding record ~50 MHz addressability for our PSP.

A spot size of $2w_0$=~300 μm was measured by scanning a 0-π abrupt spatial phase jump through the spot in the dispersion direction when excited with a CW laser using the SLM and monitoring the fiber coupled power (Fig. 3.3.1.c). Using this in the PSP resolution definition we get $\Delta\nu_{res} = w_0/(dx/d\nu) =\sim 1$ GHz, in agreement with our direct resolution measurement.

The observed loss in this setup (Fig. 3.3.3) is -12 dB. The identified loss mechanisms are as follows: WGR fiber coupling efficiency (×2) -6.5 dB, and LCoS SLM -2 dB. The total known loss amounts to -8.5 dB, leaving unaccounted losses of 3.5 dB that are likely from inefficiency of optical collimation and focusing back to WGR We noticed that the insertion loss of the WGR increased by 0.7 dB after the trimming process, from -2.5 to -3.2 dB. This might be due to light scattering from the dilated waveguide cladding.

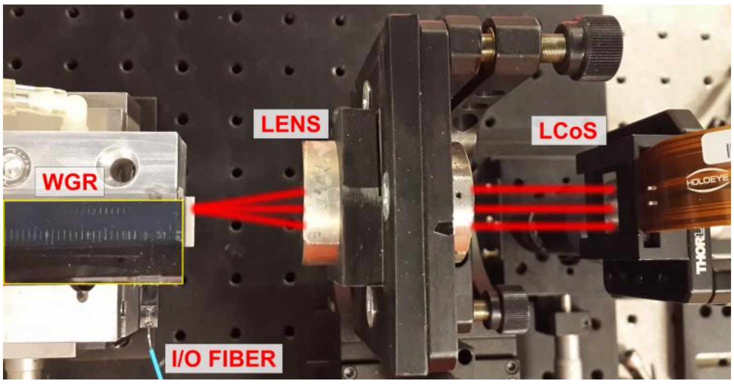

Figure 3.3.3 PSP set-up consisting of WGR, Fourier lens, and LCoS SLM only.

3.4 Discussion and Conclusions

In this thesis we introduced a fine resolution Photonic Spectral Processor (PSP), built upon a 25 GHz WGR that underwent permanent phase error corrections via a UV excimer laser. The optical filtering arrangement is greatly simplified thanks to the phase-corrected WGR, and is compact and robust.

We first developed a fully automated WGR scanning and phase evaluation procedure. Showing we can measure WGR phase errors with high repeatability we assessed the amount of phase trim required by each waveguide. We then developed a trimming procedure, and managed to achieve a permanent compensation of the WGR manufacturing errors.

We finished with assembling a PSP using the phase-corrected WGR. The PSP’s spectral filtering ability was provided by an LCoS SLM in the Fourier plane, enabling us to create a 12.5/25 GHz interleaver, and a flexible selection of passband bandwidths (Fig. 3.3.2). Optical losses of 12 dB can be improved further by eliminating circulator, better free space optics and optical alignment.

Due to polarization dependent errors and trimming, this error correction method requires polarization diversity, which may be added by additional WGR in a stacked configuration. In addition, the amount of trimming repetitions needed for this correction method makes it more feasible for WGRs with small number of waveguide arms.

4. References

1. D. M. Marom, et al., “Wavelength-selective 1×2 switch utilizing a planar lightwave circuit stack and a MEMS micromirror array,” Proc. Optical MEMS 2004, Takamatsu, Japan, Aug. 2004.
2. T. Ducellier, et al., “Novel High Performance Hybrid Waveguide-MEMS 1x9 Wavelength Selective Switch in a 32-Cascade Loop Experiment,” Proc. of ECOC 2004, Th4.2.2.
3. N. Ooba, et al., “Compact Wide-Band Wavelength Blocker Utilizing Novel Hybrid AWG-Free Space Focusing Optics,” Proc. Opt. Fiber Comm. (OFC) 2008 San Diego, Paper OWI2.
4. D. Sinefeld and D. M. Marom, “Spectral Processor Implemented with Hybrid Free-Space and Guided-Wave Optics and Active LCoS Modulator,” Proc. IEEE Israel 2008, Eilat, Israel, 2008.
5. J. E. Ford, V. A. Aksyuk, D. J. Bishop, and J. A. Walker, “Wavelength Add-Drop Switching Using Tilting Micromirrors,” J. Lightwave Technol. 17, 904-911, 1999.
6. D. M. Marom, et al., “Wavelength-Selective 1×K Switches using Free-Space Optics and MEMS Micromirrors: Theory, Design, and Implementation,” IEEE J. Lightwave Technol. 23, 1620-30, 2005.
7. D. Sinefeld and D. M. Marom, “Hybrid Guided-Wave/Free-Space Optics Photonic Spectral Processor Based on LCoS Phase Only Modulator,” Photon. Technol. Lett. 22, 510-512, 2010.
8. K. Seno, et al., “50-Wavelength Channel-by-Channel Tunable Optical Dispersion Compensator Using a Combination of AWG and Bulk Grating,” Photon. Technol. Lett. 22, 1659-1661, 2010
9. D. Sinefeld, C. R. Doerr, and D. M. Marom, "A photonic spectral processor employing two-dimensional WDM channel separation and a phase LCoS modulator," Opt. Express 19, 14532-14541, 2011.
10. T. Kamalakis, T. Sphicopoulos, and D. Syvridis, “An estimation of performance degradation due to fabrication errors in AWGs,” J. Lightwave Technol. 20 (9), 1779–1787, 2002.

11. K. Takada, Y. Inoue, H. Yamada and M. Horiguchi, “Measurement of phase error distributions in silica abased arrayed-waveguide grating multiplexers by using Fourier transform spectroscopy,” Electron. Lett. 30, 1671-1672, 1994.
12. K. Takada, M. Abe, T. Shibata, and K. Okamoto, “1-GHz-spaced 16-channel arrayed-waveguide grating for a wavelength reference standard in DWDM network systems,” J. Lightwave Technol. 20, 850-853, 2002.
13. Noam Goldshtein, Leonid Pascar, Roy Rudnick, David Sinefeld, Ori Golani, Roy Zektzer, and Dan M. Marom “Fine Resolution Photonic Spectral Processor Using a Waveguide Grating Router with Permanent Phase Trimming," J. Lightwave Technol. ,accepted Nov. 2015 paper JLT-18092-2015.R1.
14. M. Shirasaki, “Chromatic dispersion compensator using virtually imaged phased array,” IEEE Photon. Technol. Lett. vol. 9, no. 12, pp. 1598-1600, Dec 1997.
15. A. Agmon, et al., “OFDM/WDM PON With Laserless, Colorless 1 Gb/s ONUs Based on Si-PIC and Slow IC,” J. Opt. Commun. Netw. 6 (3), 225-237, 2014.
16. D. Sinefeld, N. Goldshtein, R. Zektzer, N. Gorbatov, M. Tur, and D. M. Marom, “Output Radiating Waveguide grating router: Characterization of Phase Errors and UV Trimming,” Bragg Gratings, Photosensitivity, and Poling in Glass Waveguides (BGPP), Colorado Springs, CO, USA, June 2012.
17. D. L. Williams, et al., “Direct observation of UV induced bleaching of 240nm absorption band in photosensitive germanosilicate glass fibres,” J. Electronics Letters 28 (4), 369-371, 1992.
18. J. Hubner, J.M. Jauanno, J.E. Pedersen, R. Kromann, T. Feuchter, M. Kristensen “Strong Bragg gratings in non-sensitized low loss planar waveguides as building blocks for WDM network component”, Phosensitive Optical Materials& Devices, SPIE 2998, 142-147, (1997).
19. R.M. Atkins, P. J. Lemaire, T. Erdogan and V Miarahi, “Mechanisms of enhanced UV photosensitivity in Germanosilicate glasses, Electron. Lett., 29 (14) ,1234-1235, 1993
20. H. N. J. Fernando, J. Canning, L. Wosinski, B. Jaskorzynska, and M. Dainese, “Characterization of ultra-violet-induced changes in planar waveguides,” J. Opt. A: Pure Appl. Opt. 5, 335–340, 2003.
21. F. Kherbouche, et al., “UV-induced stress field during Bragg grating inscription in optical fibres”, J. Opt. A: Pure Appl. Opt. 3, p. 429–439, 2001.

22. Abe, M.; Hibino, Y.; Tanaka, T.; Itoh, M.; Himeno, A.; Ohmori, Y., "Mach-Zehnder interferometer and arrayed-waveguide-grating integrated multi/demultiplexer with photosensitive wavelength tuning,", Electronics Letters , vol.37, no.6, pp.376-377, 15 Mar 2001

Appendix:

Appendix: Spatial Light Modulator

Commercially available Liquid Crystal on Silicon (LCoS) Spatial Light Modulators (SLM) enable amplitude and phase control by manipulating the phase of light incident on the LCoS panel (Fig. 5.1). Thanks to developments in the display industry, this type of SLM has a high resolution modulator arrays that can be utilized for WDM spectral manipulations.

A liquid crystal (LC) layer which lies between a transparent electrode and a VLSI die enables changing the refractive index of each specific pixel, by applying a voltage to rotate the LC molecules.

The angular orientation of the LC molecules is dependent on the applied voltage according to $\theta = \frac{\pi}{2} - 2\arctan(e^{-V})$ (5.1)

LC molecules are elliptic, so their rotation effects the index ellipsoid according to $\frac{1}{n(\theta)^2} = \frac{\cos^2(\theta)}{n_0^2} + \frac{\sin^2(\theta)}{n_e^2}$ (5.2), where n_o and n_e are the index of refraction of the ordinary and extra-ordinary axis of the LC molecule respectively. The phase that each pixel can apply is: $\varphi = \frac{2\pi d}{\lambda}\left(n(V) - n_0\right)$ (5.3), where d is the thickness of the LC layer.

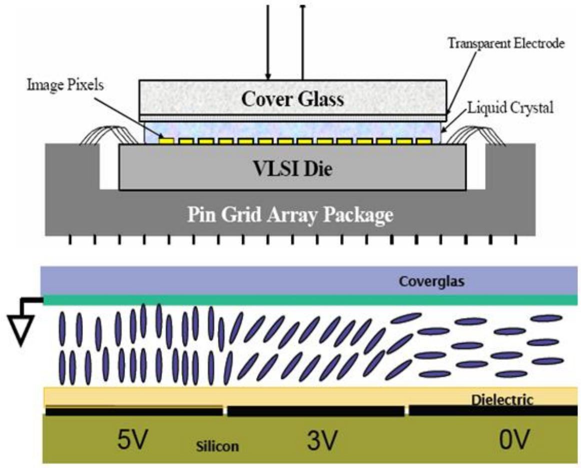

Figure 5.1 – Phase SLM basic concept of operation: a layer of liquid crystals is placed between a transparent electrode and a VLSI die of two dimensional array of pixels. Different voltage values applied separately on each SLM pixel result in different local index of refraction. This change is equal to a change in the optical path length (OPL) and therefore to a phase delay. In this way one can prescribe a two dimensional phase along the SLM plane.

Our PSP uses a commercially available Holoeye Pluto LCoS phase modulator with high definition (HD) resolution of 1080×1920, pixels of 8 μm pitch, and total active size of 15.36×8.64 mm. It is designed to work around the 1550nm region, with a phase modulation range of up to 2π at.

Phase patterns with modulation of more than 2π can be prescribed by applying a modulo 2π phase which is mathematically identical to the original phase. The performance of the SLM is limited to the number of pixels, and the number of controllable gray levels.